



HHS Public Access

Author manuscript

Nat Commun. Author manuscript; available in PMC 2013 April 03.

Published in final edited form as:

Nat Commun. ; 3: 778. doi:10.1038/ncomms1777.

Nanodomain Ca^{2+} of Ca^{2+} channels detected by a tethered genetically encoded Ca^{2+} sensor

Lai Hock Tay¹, Ivy E. Dick¹, Wanjun Yang¹, Marco Mank³, Oliver Griesbeck³, and David T. Yue^{1,2}

¹Calcium Signals Laboratory, Department of Biomedical Engineering, Johns Hopkins University School of Medicine, Ross Building, Room 713, 720 Rutland Avenue, Baltimore, Maryland 21205, USA

²Calcium Signals Laboratory, Department of Neuroscience, Johns Hopkins University School of Medicine, Ross Building, Room 713, 720 Rutland Avenue, Baltimore, Maryland 21205, USA

³AG Zelluläre Dynamik, Max-Planck-Institut für Neurobiologie, Am Klopferspitz 18, 82152 Martinsried, Germany

Abstract

Coupling of excitation to secretion, contraction, and transcription often relies upon Ca^{2+} computations within the nanodomain—a conceptual region extending tens of nanometers from the cytoplasmic mouth of Ca^{2+} channels. Theory predicts that nanodomain Ca^{2+} signals differ vastly from the slow submicromolar signals routinely observed in bulk cytoplasm. However, direct visualization of nanodomain Ca^{2+} far exceeds optical resolution of spatially distributed Ca^{2+} indicators. Here we couple an optical genetically encoded Ca^{2+} indicator (TN-XL) to the carboxyl tail of $\text{Ca}_v2.2$ Ca^{2+} channels, enabling nearfield imaging of the nanodomain. Under TIRF microscopy, we detect Ca^{2+} responses indicative of large-amplitude pulses. Single-channel electrophysiology reveals a corresponding Ca^{2+} influx of only 0.085 pA, and FRET measurements estimate TN-XL distance to the cytoplasmic mouth at ~ 55 Å. Altogether, these findings raise the possibility that Ca^{2+} exits the channel through the analog of molecular portals, mirroring the crystallographic images of side windows in voltage-gated K channels.

INTRODUCTION

Ca^{2+} signals extend pervasively across the intracellular expanse of most cells, yet these signals exhibit remarkable specificity in activating appropriate Ca^{2+} -modulated targets. Understanding how this selectivity arises remains a foremost question in Ca^{2+} biology^{1,2}.

Users may view, print, copy, download and text and data-mine the content in such documents, for the purposes of academic research, subject always to the full Conditions of use: http://www.nature.com/authors/editorial_policies/license.html#terms

Author contributions

L.H.T. established the TIRF/patch-clamp apparatus, designed and performed research, analysed data, and wrote the paper. I.E.D. performed extensive electrophysiological experiments, FRET imaging, and data analysis. W.Y. performed western blots and molecular biology. M.M. and O.G. guided use of TN-XL. D.T.Y. conceived experiments and analyses, established and performed numerical simulations, analysed data, made figures, and wrote the paper.

Competing financial interests

The authors declare no competing financial interests.

One strategy is to colocalize at molecular dimensions Ca^{2+} sources and targets. This colocalization is crucial to the local signaling of Ca^{2+} channels to nearby Ca^{2+} -regulated ion channels and enzymes³⁻⁵, to neurotransmitter release⁶, as well as to excitation-contraction⁷ and excitation-transcription coupling^{8,9}. Intriguingly, colocalized sensors do not always respond preferentially to local Ca^{2+} sources, but can require the far weaker input of remote Ca^{2+} sources acting through a global Ca^{2+} selectivity paradigm¹⁰. Critical to signaling near Ca^{2+} sources is the nature of Ca^{2+} signals within a few tens of nanometers of a Ca^{2+} channel (nanodomain¹¹). Theoretical calculations¹²⁻¹⁶ postulate that nanodomain signals comprise Ca^{2+} pulses of equal and enormous amplitude ($\sim 100 \mu\text{M}$), with each pulse synchronized to the millisecond stochastic openings of channels^{10,12}. Beyond the nanodomain, $[\text{Ca}^{2+}]$ rapidly dissipates with diffusion. Of note, predicted nanodomain $[\text{Ca}^{2+}]$ amplitudes vary considerably with assumed parameters¹⁷, and elegant experimental estimates of local Ca^{2+} signals^{18,19} only indirectly probe the nanodomain itself. Thus, the critical magnitude of nanodomain Ca^{2+} pulses ($C_{a_{\text{spike}}}$) has eluded explicit empirical comment. This uncertainty bears on key issues, including how spatial Ca^{2+} decoding occurs within the nanodomain^{10,20-22}, and the Ca^{2+} channel number needed to trigger neurotransmitter vesicles²³⁻²⁵.

Why have nanodomain Ca^{2+} signals remained elusive? Though fluorescent Ca^{2+} -sensitive chemical dyes has revealed much²⁶, visualization of nanodomain signals via freely diffusible dye molecules far exceeds the resolution limit of far-field microscopic approaches²⁷. In this regime, fluorescence from dye molecules outside the nanodomain will overshadow that from within²⁸. Even when imaged with total internal reflection fluorescence (TIRF) microscopy²⁹⁻³¹, which illuminates a restricted TIRF volume within $\sim 150 \text{ nm}$ of the glass/cell membrane interface, freely diffusible dyes will still report Ca^{2+} from a region several-fold larger than a Ca^{2+} channel³².

One approach is to affix a Ca^{2+} indicator within the nanodomain, so as to support a form of near-field imaging³³. The Ca^{2+} -sensitive luminescent protein aequorin represents a traditional candidate³⁴. Recombinant aequorins have long been targeted to various subcellular compartments by genetic means³⁵⁻³⁷, but the limited-amplitude and consumptive nature of aequorin would challenge deployment in a channel nanodomain³⁴. Recently, promising results have been obtained using a biarsenical chemical fluorescent Ca^{2+} indicator (Calcium Green FAsH, CaGF) targeted to a tetracysteine tag implanted on $\text{Ca}_V1.2$ Ca^{2+} channels³⁸. CaGF features Ca^{2+} affinity and kinetics ($K_d \sim 55 \mu\text{M}$; off rate, 2 ms^{-1}) well matched to the purported amplitudes and lifetimes of nanodomain Ca^{2+} pulses. Indeed, CaGF was potentially responsive to nanodomain Ca^{2+} fluctuations, but the observed fluorescence signals were highly heterogeneous, to an extent that precluded quantitative Ca^{2+} estimation. This heterogeneity was attributable to the diminutive and variable open probability of $\text{Ca}_V1.2$ channels ($\sim 0.1-0.3\%$), despite constitutive pharmacological manipulation by a channel opener. Indeed, the possibility of a large fraction of electrically silent $\text{Ca}_V1.2$ channels fits with their unusually large ratio of gating charge to ionic current³⁹. Also, though the authors were careful to control for non-specific labeling of other cysteine-rich sites in the cell by CaGF, such indiscriminate attachment would remain a generic concern for approaches involving chemical targeting of sensors. A third approach

would be to employ genetically encoded Ca^{2+} indicators (GECIs) as near-field sensors. GECIs allow genetic fusion of sensor to a Ca^{2+} source, offering the greatest potential selectivity in positioning sensors. Among the most popular GECIs are CFP/YFP-FRET-based molecules such as cameleons⁴⁰, and GFP-intensity-based sensors like GCaMPs⁴¹. All these employ calmodulin (CaM) as their Ca^{2+} sensor, and convert binding of the sensor's own Ca^{2+} /CaM with a target peptide into altered optical readouts. When targeted to plasmalemma, cameleons often lose Ca^{2+} sensitivity⁴², potentially via target peptide binding to elevated plasmalemmal CaM⁴³.

Accordingly, we here explore nearfield imaging of nanodomain Ca^{2+} using TN-XL, a GECI⁴⁴ based on the Ca^{2+} sensor troponin C. TN-XL exploits Ca^{2+} -driven conformational changes without a target peptide, thereby naturally resisting endogenous CaM interference⁴². Our specific approach is to fuse TN-XL to the C-terminus of the principle subunit of $\text{Ca}_v2.2$ Ca^{2+} channels, chosen for high open probability⁴⁵, relative absence of silent channels⁴⁶, and abundant plasmalemmal expression⁴⁷. To further improve the TN-XL signal-to-noise ratio at the surface membrane, we utilize TIRF microscopy to selectively illuminate only those $\text{Ca}_v2.2$ /TN-XL channels near the surface, thereby attenuating background signal from imperfectly targeted intracellular channels. Finally, to account for the high Ca^{2+} affinity and slow kinetics of GECIs⁴⁴ (off times 100–900 ms for TN-XL) in the face of millisecond nanodomain Ca^{2+} pulses, we quantify the kinetics of TN-XL readouts, which our previous work suggests can distinguish between differing $C_{a_{\text{spike}}}$ amplitudes⁴⁸. These strategies allow us to resolve nanodomain Ca^{2+} activity of $\text{Ca}_v2.2$ channels undergoing native gating, without pharmacological manipulation.

RESULTS

Functional $\text{Ca}_v2.2$ /TN-XL fusions at the surface membrane

Our strategy for probing nanodomain Ca^{2+} signals (Fig. 1) requires maintained Ca^{2+} responsiveness of genetically encoded sensors situated at the plasmalemma, a foremost challenge. Accordingly, we examined whether troponin-based TN-XL could respond to Ca^{2+} when targeted to this environment. As a baseline, Fig. 2a displays the properties of the well-studied, cytoplasmic form of TN-XL⁴⁴. Confocal images of an exemplar HEK293 cell, acquired under CFP and FRET imaging modes, reveal the expected pan-cytoplasmic distribution. An epifluorescence CFP image of another cell also demonstrates this generalized expression, and switching to TIRF mode indicates no preferential TN-XL accumulation within the plasmalemmal footprint of this same cell. To gauge TN-XL responsiveness, we measured under TIRF imaging the single-cell CFP (S_C , respective excitation and emission wavelengths at 442 and 485 nm) and FRET fluorescence signals (S_F , excitation and emission at 442 and 545 nm), where the ratio of these signals ($R_{F/C} = S_F/S_C$) furnishes the customary sensor readout of Ca^{2+} (Fig. 2b). In particular, the ratio $R_{F/C}$ was first determined in resting cells with cytoplasmic Ca^{2+} concentration ($\sim 0.1 \mu\text{M}$) well below the K_d of the TN-XL²⁴, thus yielding R_{min} . To subsequently determine R_{max} , $\text{Ca}_v2.2$ channels were co-expressed as conduits of Ca^{2+} entry under whole-cell voltage clamp. To facilitate elevation of intracellular Ca^{2+} , minimal internal Ca^{2+} buffering (1 mM EGTA) with elevated 10 mM extracellular Ca^{2+} was employed, such that repetitive step

depolarizations ($30 \text{ mV} \times 500 \text{ ms}$ pulses every 15 s) readily saturated $R_{F/C}$ at R_{max} . Thus, the ratio of R_{max} and R_{min} reports sensor dynamic range.

By contrast, for TN-XL fused to the farnesylation motif of Ras (TN-XL-Ras), sensors are sharply localized to the surface membrane in confocal and epifluorescence images (Fig. 2c), and there is marked enrichment within the TIRF footprint. Importantly, the Ca^{2+} dynamic range of TN-XL-Ras is nearly identical (Fig. 2d), despite residence within the plasmalemmal context. Yet more relevant are results for the $\text{Ca}_v2.2/\text{TN-XL}$ fusions (Fig. 2e). Here, constructs appear only partially localized to the surface membrane, consistent with typically imperfect trafficking of recombinant Ca^{2+} channels to plasmalemma⁴⁹. Still, there is substantial focalization of $\text{Ca}_v2.2/\text{TN-XL}$ in the TIRF footprint, suggesting sufficient trafficking for nanodomain experiments (Fig. 1c). Critically, sensor dynamic range is spared when juxtaposed near $\text{Ca}_v2.2$ channels (Fig. 2f).

A second concern is the preservation of $\text{Ca}_v2.2$ channel function upon fusion to TN-XL. Reassuringly, Ca^{2+} currents appeared nearly identical in $\text{Ca}_v2.2/\text{TN-XL}$ (Fig. 3a, black) and $\text{Ca}_v2.2$ (gray) channels. In fact, fusing TN-XL to $\text{Ca}_v2.2$ enhances opening, as seen from hyperpolarization of tail-activation curves determined with 10 mM extracellular Ca^{2+} as charge carrier (Fig. 3b). Even at the single-channel level, $\text{Ca}_v2.2/\text{TN-XL}$ fusions exhibited robust electrophysiological function, as illustrated by the exemplar single-channel current trace shown at high-gain magnification (Fig. 3c, noisy trace). We used 90 mM Ba^{2+} as a charge carrier to enhance resolution of elementary events, and evoked currents via ramp depolarization to readily resolve the open-channel conduction profile (downwardly convex gray relation). Multiple single-channel sweeps (Fig. 3d), displayed at lower-gain magnification, confirm the overall reproducibility and excellent resolution of elementary events under this protocol. Accordingly, numerous sweeps from multiple patches specify a highly reliable ensemble average current (Fig. 3c, red curve), closely similar to that of $\text{Ca}_v2.2$ channels without sensor fusion⁴⁵. Taking a ratio of the ensemble average current with the open-channel conduction profile (Fig. 3c, red and convex gray curves) yields a plot of open probability P_O versus voltage V (Fig. 3e, gray relation). This plot matches impressively with whole-cell activation (reproduced as open circles), after shifting along the voltage axis to account for contrasting surface-charge effects of single-channel versus whole-cell solutions. As with studies of $\text{Ca}_v2.2$ ⁴⁵, the $\text{Ca}_v2.2/\text{TN-XL}$ fusion exhibits a substantial P_O of 0.69 at 30 mV (Fig. 3e, red arrows), a feature advantageous for probing nanodomain Ca^{2+} .

A final prerequisite is that $\text{Ca}_v2.2/\text{TN-XL}$ fusions resist proteolysis. Accordingly, we utilized anti-GFP antibody to perform western immunoblots from cells expressing this construct (Fig. 3f, left lane). The other lanes correspond to cells expressing TN-XL-Ras (~71 kD), as well as untransfected cells (no signal). The absence of signal beneath the full-length ~320 kD band (Fig. 3f, left lane) substantiates maintained TN-XL fusion to channels (Fig. 3g).

Calibration of TN-XL fused to $\text{Ca}_v2.2$ channels

We next addressed more precise sensor calibration, to facilitate quantitative inferences about nanodomain Ca^{2+} . Both kinetic and steady-state characterization would be ideal, given the

millisecond kinetics of Ca^{2+} pulses within channel nanodomains, coupled with the comparatively slow response of free TN-XL (off rates of 1/150 to 1/850 1/ms⁴⁴). Accordingly, we devised a state-mechanism approximation of sensor performance, a ‘forward transform’ that maps rapid Ca^{2+} transient inputs onto slower sensor outputs, as previously established for an older variant of TN-XL (TN-L15) freely expressed in myocytes⁴⁸. Here, we pursued an analogous approach, but attuned to $\text{Ca}_v2.2/\text{TN-XL}$ constructs resident within the TIRF volume and driven by high-amplitude dynamic Ca^{2+} inputs pertinent to channel nanodomains. To produce such inputs, we activated ultra-large $\text{Ca}_v2.2$ Ca^{2+} currents (Fig. 4a) in HEK293 cells featuring minimal exogenous intracellular Ca^{2+} buffering (1 mM EGTA); this configuration intentionally produced enormous spatial gradients of intracellular Ca^{2+} (Fig. 4b inset), far exceeding that usually encountered. To estimate these gradients, we simultaneously monitored aggregate Ca^{2+} concentration (Fig. 4b, noisy dark trace), as deduced by imaging the entire cell for signals emanating from 10 μM of the rapid chemical fluorescent Ca^{2+} indicator Fluo 4FF. The measured Ca^{2+} influx (Fig. 4a) and aggregate $[\text{Ca}^{2+}]$ signals were then used to explicitly constrain a radially symmetric Ca^{2+} diffusion mechanism, whose estimates of Ca^{2+} concentration in differing cellular regions are shown as red traces in Fig. 4b (Supplementary Figure S1 and Supplementary Methods). The estimated aggregate $[\text{Ca}^{2+}]$ concentration (Fig. 4b, lower red trace) closely approximates its measured analog (dark noisy trace), and the estimated $[\text{Ca}^{2+}]$ at the surface membrane (upper red trace) peaks at $\sim 80 \mu\text{M}$ and later converges to the aggregate $[\text{Ca}^{2+}]$ ($\sim 20\text{--}25 \mu\text{M}$). This estimate of submembranous $[\text{Ca}^{2+}]$ was reproducible in multiple cells exhibiting like Ca^{2+} influx, and was thereby taken as the relevant Ca^{2+} input in parallel experiments performed with $\text{Ca}_v2.2/\text{TN-XL}$ fusion constructs under TIRF imaging. The green trace in Fig. 4c displays the corresponding sensor output from GECIs in the submembranous TIRF volume, averaged from multiple cells exhibiting Ca^{2+} influx matching that in Fig. 4a. The steady-state plateau of the response (Fig. 4c, gray dashed line at $R_{F/C} = 1.78$), at a near steady Ca^{2+} concentration of $\sim 20\text{--}25 \mu\text{M}$, enabled us to calculate $\sim 17.3 \mu\text{M}$ as the half-response point of the steady-state response curve for $\text{Ca}_v2.2/\text{TN-XL}$ constructs in the TIRF volume (Supplementary Methods). This differs from the $2.5 \mu\text{M}$ half response point for free TN-XL⁴⁴, consistent with prior observations that sensor performance can change with cellular/molecular environment^{38,42}. Accordingly, steady-state response data for free TN-XL⁴⁴ were shifted along the $[\text{Ca}^{2+}]$ axis by $\times 16.3/2.5$ to provide an appropriate steady-state profile for $\text{Ca}_v2.2/\text{TN-XL}$ constructs (Fig. 4d, green symbols). In all, these steady-state data and the dynamic sensor response (Fig. 4c, green trace) to a specified submembranous Ca^{2+} input (Fig. 4b, upper red trace) furnished the constraints required to deduce a forward transform for $\text{Ca}_v2.2/\text{TN-XL}$.

Fig. 4e displays the corresponding state-diagram approximation of $\text{Ca}_v2.2/\text{TN-XL}$ responsiveness to Ca^{2+} , based upon a mechanism for an older troponin-based GECI⁴⁸ (TN-L15). State UB_0 (‘unbound’) represents the Ca^{2+} -free conformation of the sensor, characterized by a lower FRET-ratio output of R_{min} . Upon binding of a single Ca^{2+} to the N-lobe of troponin, the sensor adopts one of two alternate ‘bound’ conformations (B_1 or B_2), both featuring the same elevated FRET-ratio output of R_{mid} . The arrangement thus far is identical to that previously established for TN-L15⁴⁸. The improved performance of TN-XL arises via engineering the C-lobe of troponin to dynamically bind and unbind two signaling

Ca²⁺ ions, thereby driving a further conformational change of the sensor⁴⁴. To account for this feature, we allowed two additional Ca²⁺ ions to bind and induce a third bound state^{50,51} (B₃, dashed box), exhibiting the highest FRET-ratio output of R_{\max} . Numerical simulations of this scheme (Supplementary Methods), coupled with error minimization via parameter variation, yielded impressive fits to the target constraints above (Figs. 4c and 4d, red curves), using the sensor parameter estimates in Table 1. Accordingly, these parameters and the scheme in Fig. 4e furnish a steady-state and dynamic representation of Ca_v2.2/TN-XL responsiveness to Ca²⁺, a ‘forward transform’ (Fig. 4f) potentially appropriate for making inferences about channel nanodomain Ca²⁺ fluctuations.

Ca_v2.2/TN-XL sensors respond to nanodomain Ca²⁺ signals

This transform could only be utilized, however, if a substantial fraction of Ca_v2.2/TN-XL sensors respond to channel nanodomain Ca²⁺ signals, as specifically produced by individual channels fluxing Ca²⁺ into their own nanodomain. Thus far, we had only demonstrated that Ca_v2.2/TN-XL sensors in the TIRF volume respond well to a generalized increase in submembranous [Ca²⁺], but this would occur whether the majority of channel-sensor fusion constructs are properly trafficked to the surface membrane, or still plentiful in submembranous vesicles within the TIRF volume. To address this issue, we again undertook simultaneous recordings of whole-cell Ca²⁺ current and TIRF imaging of Ca_v2.2/TN-XL sensors, but here with high intracellular Ca²⁺ buffering present to restrict Ca²⁺ elevations to the nanodomain of active channels that flux Ca²⁺. Specifically, we dialyzed cells with 10 mM EGTA, yielding a Ca²⁺ nanodomain radius of ~40 nm¹³ (Fig. 5), only two-fold larger than electron micrographic estimates of Ca²⁺ channel diameters³². Additionally, we only investigated cells with modest Ca²⁺ currents (~1 nA with 10 mM Ca²⁺ as charge carrier) and little Ca²⁺-dependent inactivation²¹ (CDI), so as to exclude Ca²⁺ buffer depletion. Fig. 5a summarizes the results of an exemplar cell satisfying this criterion, with the displayed data evoked by a single voltage pulse. Clearly present is a transient decrease in CFP fluorescence (S_C , cyan trace), accompanied by a corresponding phasic elevation of the FRET ratio $R_{F/C}$ (green trace). Exponential fits (solid black curves) revealed dominant rise and fall times of 880 and 2000 ms for S_C , and 880 and 400 ms for $R_{F/C}$. Both the return of TN-XL waveforms towards baseline, and the modest CDI of channels under elevated Ca²⁺ buffering²¹ (Fig. 5a compared to Fig. 4a), argue against unintended depletion of Ca²⁺ buffer. Accordingly, these results suggest responsiveness of Ca_v2.2/TN-XL sensors to genuine channel nanodomain Ca²⁺ signals. By contrast to the exemplar, about half the cells with currents of this magnitude and limited CDI exhibited no appreciable change of TN-XL readouts, presumably due to poor trafficking of active channels. Such cells were excluded from further analysis.

Forward transform estimates of nanodomain Ca²⁺ amplitudes

As a prelude to more rigorous assessment of Ca_v2.2/TN-XL responses to nanodomain signals, we averaged signals from multiple responsive cells dialyzed with 10 mM EGTA. The mean responses (Fig. 5b) were similar to those of the exemplar, with nearly identical characteristic time constants. This reproducibility encouraged us to quantitatively scrutinize these averaged waveforms. In particular, while the robust responses observed here under elevated Ca²⁺ buffering do indicate an appreciable fraction of active channels within the

TIRF volume (Fig. 5c, active), the data do not exclude the possibility of a still substantial fraction of channels that are present in the plasmalemma but fail to open (Fig. 5c, silent), or resident within submembranous vesicles within the TIRF volume (Fig. 5c, intracellular). Such silent and/or intracellular channels would contribute static background fluorescence that could complicate quantitative interpretation. An indication of this scenario comes from exponential extrapolation of the S_C waveform decline (Fig. 5b, dashed curve), which asymptotes in the range of ~ 0.8 . By contrast, under the assumption that all channels are active, simulations of the forward transform in Figs. 4e and 4f indicate that, over a large range of plausible nanodomain Ca^{2+} pulse amplitudes ($< 35 \mu M$), S_C waveforms would asymptote near Ca^{2+} -saturating levels of ~ 0.5 (Supplementary Figure S2, Supplementary Methods), as specified by the experimentally determined $1/\alpha_0$ value (defined in Table 1). Hence, the experimentally deduced asymptote of ~ 0.8 (Fig. 5b) suggests that $\sim 40\%$ of $Ca_V2.2/TN-XL$ channels are active within the TIRF volume, while $\sim 60\%$ of channels are intracellular or silent. Cognizant of this configuration, we correct S_C and $R_{F/C}$ waveforms to reflect only active channels, simply by subtracting $\sim 60\%$ of the baseline amplitude of CFP (S_C) and FRET (S_F) signals, and taking a ratio of these subtracted signals to obtain a corrected $R_{F/C}$. Fig. 6a shows the corrected signals (S_C , $R_{F/C}$), averaged over multiple cells. These waveforms were then suitable for making inferences about nanodomain Ca^{2+} .

That nanodomain Ca^{2+} signals take the form of equi-amplitude Ca^{2+} pulses synchronized to the millisecond opening of channels is widely accepted^{10,12} (cartoon, Fig. 6b); however, the critical amplitude of such pulses (Ca_{spike}) has only been inferred via simulations of Ca^{2+} diffusion¹²⁻¹⁶. To estimate Ca_{spike} empirically, we analyzed the corrected $Ca_V2.2/TN-XL$ responses (Fig. 6a) using the forward transform in Figs. 4e and 4f. The experimental waveforms might initially appear difficult to conceptualize, since each TN-XL sees a different stochastic record of Ca^{2+} pulses driven by single-channel openings. However, because the response of each TN-XL is slow (Table 1, compare Figs. 4b, 4c) relative to the millisecond duration of individual Ca^{2+} spikes, we can adopt a previously established kinetic simplification¹⁰ that permits the Ca^{2+} -driven forward reaction rates in Fig. 4e to be treated, not as stochastic entities that fluctuate with each Ca^{2+} pulse, but as smoothly changing entities $k_{01} \cdot Ca_{spike} \cdot P_O(t)$ and $k_{23} \cdot Ca_{spike}^2 \cdot P_O(t)$. Importantly, these entities are to the first order equal for all active $Ca_V2.2/TN-XL$ sensors, such that the collective output from multiple sensors, as displayed in Fig. 6a, would approximate that for any individual sensor on average. Thus, using our forward transform (Figs. 4e and 4f) to predict experimental waveforms becomes simple. Single-channel data (Fig. 3e) permit average whole-cell currents (Fig. 5b) to be rescaled as an open probability P_O waveform (Figs. 6a and 6b); this P_O drives straightforward numerical integration of the differential equations corresponding to the transform in Fig. 4e; and this integration yields predictions of experimental waveforms, with the magnitude of Ca_{spike} being the only unknown (Supplementary Methods). While presumed Ca_{spike} values of 15 or 240 μM yield predicted $R_{F/C}$ trajectories (Fig. 6a, gray smooth curves) that are patently inconsistent with the experimental curve, $Ca_{spike} = 60 \mu M$ produces an impressive fit to data (smooth red curves). Indeed, error analysis (Fig. 6c) confirms 60 μM as a best estimate of Ca_{spike} . As a conservative lower limit, we performed transform analysis on uncorrected waveforms (Fig. 5b), yielding a still-large estimated $Ca_{spike} \sim 15 \mu M$ (Supplementary Figure S3,

Supplementary Methods). Fits to uncorrected data were notably inferior, further prompting us to favor Ca_{spike} estimates from the background-corrected data in Fig. 6a. For these data, the shading in Fig. 6c encompasses fits with errors similar to the minimum, yielding an approximate Ca_{spike} range of 45–80 μM . This estimate, combined with determination of the underlying single-channel current amplitude, can potentially furnish valuable insight into Ca^{2+} diffusion properties within the nanodomain itself (Fig. 7).

DISCUSSION

The fusion of $\text{Ca}_v2.2$ channels to the genetically encoded Ca^{2+} sensor TN-XL here furnishes a new tool for detecting submembranous Ca^{2+} signals near these ‘N-type’ Ca^{2+} channels (Fig. 1b). Our particular application concerns the nanodomain Ca^{2+} transients accompanying individual channel openings and closings. These transients have eluded direct experimental comment until the recent advent of TIRF microscopy to image single-channel activity^{30,31}, and the availability of targetable chemical-fluorescent Ca^{2+} indicators³⁸. Here we demonstrate an alternative approach exploiting TIRF/patch-clamp electrophysiology and our $\text{Ca}_v2.2/\text{TN-XL}$ fusion. This tactic yields a first empirical estimate of the amplitude of nanodomain Ca^{2+} pulses (Ca_{spike}). This entity figures crucially in the Ca^{2+} activation of co-localized channels and enzymes², evoked release of nearby neurotransmitter vesicles²⁵, and excitation-transcription coupling^{8,9}.

A limitation of the present study concerns the incomplete targeting of active $\text{Ca}_v2.2/\text{TN-XL}$ channels to the surface membrane in the TIRF volume, necessitating approximate correction of static background fluorescence. The potential error in such correction renders our Ca_{spike} determination as a coarse approximate estimate. Nonetheless, the approach taken will prove valuable as means to improve channel trafficking arise, and GECI technology progresses.

With this proviso, we consider other long-sought-after Ca^{2+} channel signaling properties that could, in principle, be accessed with our strategy. First, we estimate the gain factor A , defined as the ratio of Ca_{spike} to unitary current i fluxing through individual Ca^{2+} channels¹². As such, the magnitude of A is crucial for local Ca^{2+} channel signaling to downstream nanodomain targets. Given knowledge of Ca_{spike} , we could estimate A itself, so long as the i were known under the conditions of Ca_{spike} determination (Fig. 6, with 10 mM Ca^{2+} as the charge carrier). The single-channel data thus far (Figs. 3c, 3d) were obtained with 90 mM Ba^{2+} to facilitate resolution of open probability; these data could not be utilized here. The relevant single-channel data for parameter A specification would entail several-fold smaller signals^{25,52}. Nonetheless, despite signals near the limits of detection, we acquired well-resolved unitary currents under these conditions (Fig. 7a). These data yield $i = 0.085 \pm 0.003$ pA ($n = 5$ patches) at 30 mV (as in Fig. 6), resembling values recorded in native $\text{Ca}_v2.2$ channels²⁵. Combining i with our estimates of Ca_{spike} (center ~ 60 μM ; range 45–80 μM), we obtain $A \sim 700$ $\mu\text{M}/\text{pA}$ (Fig. 7b, shaded regions).

Second, if the distance from the cytoplasmic mouth of the channel to the sensor (r_{sensor}) were also known, nearfield Ca^{2+} sensing could comment powerfully on Ca^{2+} diffusion within the nanodomain itself. We therefore gauge r_{sensor} from FRET measured between the CFP of our $\text{Ca}_v2.2/\text{TN-XL}$ fusion, and YFP fused to the base of the channel amino terminus

(Fig. 7c). To eliminate crosstalk, YFP within TN-XL itself is replaced with the inert analog *amber*⁵³. FRET efficiency was thus determined⁵⁴ (Fig. 7d), yielding an estimated $r_{\text{sensor}} \sim 55$ Å (Methods).

With both parameter A and r_{sensor} in hand, we scrutinize nanodomain Ca^{2+} diffusion via classic point-source Ca^{2+} diffusion, as given by a generalized Neher-Stern equation^{13,16}

$$A = \frac{C a_{\text{spike}}}{i} = \frac{(1/f)}{4 \cdot \pi \cdot F \cdot D_{\text{Ca}} \cdot r_{\text{sensor}}} \cdot \exp \left[\frac{-r_{\text{sensor}}}{\sqrt{D_{\text{Ca}} / (k_{\text{Bon}} \cdot B_{\text{T}})}} \right] \quad (1)$$

where r_{sensor} is the distance of the TN-XL sensor from the point source of Ca^{2+} influx, D_{Ca} is the diffusion coefficient of free Ca^{2+} , F is Faraday's constant, k_{Bon} is the on rate for Ca^{2+} binding to EGTA, and B_{T} is the internal EGTA concentration (10 mM). The parameter f , specifying the fraction of half-infinite space into which radial Ca^{2+} diffusion occurs, has always been set at unity (Ca^{2+} diffuses into a full half-infinite space), absent any evidence to the contrary. Intriguingly, our estimates of A and r_{sensor} square poorly with the traditional view (Fig. 7e, dashed curve with $f = 1$), but fit well with $f \sim 0.53$ ($0.53 \times 2\pi$ steradians, solid curve). This outcome may represent an early functional indication of fenestrated Ca^{2+} egress from the channel into cytoplasm (Fig. 7f), according with crystallographic structures of K channels⁵⁵.

Thus, nanodomain Ca^{2+} diffusion could focus Ca^{2+} through particular molecular geometries within the channel-signaling complex, raising the possibility of enhanced preferential signaling to target molecules near or within exit portals (Fig. 7f, gray ball). Indeed, while prior studies elegantly suggest that distinctive unitary current amplitudes i render $\text{Ca}_v2.2$ channels favorable for triggering vesicle fusion²⁵, it is also plausible that differing A and f values also factor into such optimization. The latter possibilities represent an intriguing, but nearly unexplored realm of Ca^{2+} biology. Though other interpretations are certainly viable, further empirical estimates of $C a_{\text{spike}}$, parameter A , and r_{sensor} will likely aid in this field of inquiry.

Methods

Molecular biology

$\text{Ca}_v2.2/\text{TN-XL}$ ($\text{Ca}_v2.2$ is of human origin (NM000718)) fusion construct was made by PCR, using fusion primers. Pfu polymerase (Stratagene) was used for fidelity. To make $\text{Ca}_v2.2/\text{TN-XL}$, we first generated a $\text{Ca}_v2.2$ channel with the C-terminus truncated at the 2180th amino acid and without the stop codon, $\text{Ca}_v2.2$ 2180 stopless/XbaI in pcDNA3.1. This was made by cutting $\text{Ca}_v2.2$ with Xho I and Xba I, and replacing the resulting fragment with the PCR product amplified from $\text{Ca}_v2.2$ between the Xho I and 2180th amino acid sites using forward primer CGCATCAGTTACAATGACATG, and reverse primer CTGTCTAGAAGCACCAGATGTTGA CAGCA. Next, TN-XL was PCR-amplified with an Xba I site upstream of CFP (ATG removed) and a Nhe I/Spe I site downstream of the stop codon of Citrine. The forward and reverse primers used were CGGCCGCCACCTCTAGAGTGAGC, and CAGACTAGTGCTAGCTTAGTCCTC

GATGTTGTGGC respectively. Finally, the TN-XL PCR fragment was spliced into the $Ca_v2.2$ 2180 stopless/XbaI construct at the Xba I site to give our $Ca_v2.2$ /TN-XL construct. For the variant construct in Fig. 7c, the circularly permuted Citrine in TN-XL was replaced with circularly permuted *amber*⁵³, and YFP fused to the amino terminus of $Ca_v2.2$ after removal of the first 81 amino acids²² (nearly the entire amino terminus).

Verification by complete sequence analysis of regions subjected to PCR was performed.

HEK293 cell culture and transfection

HEK293 cells were cultured on No-1 25 mm glass cover slips (Bellco glass) in 10 cm plates. These slips were coated overnight with 0.01% (wt/v; diluted 1:5 in 0.1 M Borate buffer) poly-D-lysine (Sigma), and washed with ddH₂O on the day cells were seeded onto the slips. The poly-D-lysine coating facilitates proper whole-cell voltage control at the membrane/glass interface⁵⁶, and also increases electrostatic attraction between the glass surface and cells, thus favoring cell attachment and optimal TIRF imaging. Cells were transiently transfected, using calcium-phosphate precipitation⁵⁴, with $Ca_v2.2$ /TN-XL, rat brain β_{2a} ⁵⁴, and rat brain $\alpha_{2\delta}$ ⁵⁴ (10 μ g each). $Ca_v2.2$ and β_{2a} -CFP were substituted for $Ca_v2.2$ /TN-XL and β_{2a} respectively in some experiments. Cotransfection of channels with a number of molecules did not appreciably improve channel trafficking in our system: PI3K and Akt/PKB⁵⁷, ORL receptors⁵⁸, and dominant-negative dynamin⁵⁹. TN-XL and TN-XL-Ras sensors were transfected using FuGENE6 (Roche).

Electrophysiology

Whole-cell and single-channel current records were obtained at room temperature 1–3 d post-transfection using patch-clamp amplifiers Axopatch 200B and Axopatch 200A (Axon Instruments), respectively.

For whole-cell recordings, the cells were bathed in external solution containing (in mM): TEA-MeSO₃, 140; HEPES (pH 7.4 with TEA-OH), 10; and CaCl₂, 10; at 300 mOsm, adjusted with glucose. The internal solution contained (in mM): Cs-MeSO₃, 114–135; CsCl₂, 5; EGTA, 1 or 10; MgCl₂, 1; MgATP, 4; and HEPES (pH 7.4 with CsOH), 10; 295 mOsm with Cs-MeSO₃. In some experiments, 10 μ M Fluo 4FF and 2.5 μ M Alexa 568 (Invitrogen, Molecular Probes) were included for ratiometric Ca²⁺ determination. Electrodes were pulled from borosilicate glass capillaries (WPI MTW 150-F4) and had pipette resistances ranging from 1.5–2.5 M Ω before 75% series resistance compensation. Voltage pulses were applied at 90 sec intervals. Currents were filtered at 5 kHz, and digitized at 25 kHz. Leak and capacitance transients subtracted by P/8 protocol. Data acquired and analyzed with custom MATLAB scripts (Mathworks, Natick, MA).

Single-channel recordings were all conducted in the on-cell configuration. The bath contained (in mM): K Glutamate, 132; KCl, 5; NaCl, 5; MgCl₂, 3; EGTA, 2; glucose, 10; and HEPES (pH 7.4 adjusted with KOH), 20; at 300 mOsm adjusted with glucose. This bath solution zeroed the membrane potential. The pipette solution contained, (in mM): BaCl₂, 90; TEA-MeSO₃, 20; HEPES (pH 7.4 adjusted with TEA-OH), 10; at 300 mOsm, adjusted with TEA-MeSO₃. In some experiments, 10 mM CaCl₂ was substituted for BaCl₂ and TEA-

MeSO₃ correspondingly increased. To minimize electrical noise, 5–20 MΩ patch pipettes were pulled from ultra-thick-walled (2 mm outer diameter, 1.16 mm inner diameter) borosilicate glass (BF200-116-10, Sutter Instruments), and coated with Sylgard. Seal resistance was ~80 GΩ. Voltage pulses applied at repetition intervals of 5–15 s; data sampled at 70 μsec intervals, and filtered at 2 kHz (Fig. 3c, d) or 700 Hz (Fig. 7a).

TIRF microscopy

On the day of experiments, the cover slips on which cells were cultured were mounted on a custom bath chamber for TIRF imaging. Fluorescence measurements of single cells were performed on a Nikon Eclipse TE2000U microscope, equipped with a Plan Apo 60 × TIRF objective (NA 1.45 oil immersion). Nikon immersion oil, with $n_d = 1.515$ (23 °C) was used. For TN-XL imaging, CFP excitation was delivered by a 16-mW Melles Griot 561CS 442-nm diode laser. For Fluo 4FF/Alexa 568 imaging, excitation was delivered by a 40-mW Melles Griot IMA100 argon laser featuring a 514-nm line. For TN-XL imaging, the optical path diagrammed in Supplementary Figure S4 was used, as described below. A high-resolution CoolSNAP HQ CCD camera (Photometrics), driven by IPLab (Scanalytics) scientific imaging software, was used for cell orientation and verification under TIRF microscopy. Fast quantitative data, averaged across single cells, were instead acquired via PMTs, as follows. Single-cell fluorescent signals was selected by the image-plane pinhole in a D-104C dual-channel photometer (PTI), and sent to a dichroic mirror (510dclp) which divides the fluorescence emission signals into CFP and FRET signals. These two signals passed through their respective emitters (HQ485/30m and HQ545/40m, Chroma), before being captured by two Hamamatsu R1527 PMTs. Fluorescent signals were filtered at 2 kHz and sampled at 25 kHz, and reflect the activity of several thousand Ca_v2.2/TN-XL molecules. Shutter control, dark current subtraction, and data acquisition were controlled by custom MATLAB programs. For Fluo 4FF/Alexa 568 imaging, the optical path was modified slightly. Single-cell fluorescence was isolated via the same pinhole and then sent to a dichroic mirror (545 dclp) which parsed signals into Fluo 4FF and Alexa 568 signals. These two signals passed through their respective emitters (545/40 nm bandpass and HQ580 nm lp, Chroma), before being captured by the same PMTs. The apparent K_d for Fluo 4FF/Alexa 568 ratios under our recording conditions was 20 μM, as determined in live HEK293 cells dialyzed with Ca²⁺ dye and a series of calibrated [Ca²⁺] internal solutions.

Widefield FRET microscopy

³³FRET efficiency determination, along with estimation of the ratio of donor to acceptor molecules, was performed within individual live HEK293 cells imaged through a image-plane pinhole according to CFP, FRET, and YFP filter cubes⁵⁴. Moreover, r_{sensor} in Fig. 7d was estimated using a Forster distance of 49 Å⁵⁴.

Immunoblots

HEK293 cells expressing Ca_v2.2/TN-XL or TN-XL-Ras were washed and harvested with PBS, centrifuged, and resuspended in lysis buffer (20 mM Tris-HCl [pH 7.5], 300 mM sucrose, 1 mM DTT and protease inhibitor cocktail (Roche)). Lysis was completed with freeze-thaw cycles and sonication. Membrane proteins were separated by initial

centrifugation (16,000g \times 10 min at 4°C), followed by solubilizing the resulting pellet in 1% Triton X-100. This solution was then subjected to centrifugation (16,000g \times 10 min at 4°C), yielding membrane proteins in the supernatant. Membrane proteins were denatured (95°C \times 1 min) upon dilution with TGS buffer (Bio-Rad), and resolved by 5% SDS-PAGE with no CaCl₂ added to the gel. Proteins were transferred to nitrocellulose membranes (Bio-Rad) by cooled transfer (Tris/Glycine transfer buffer/pH 8.3 \times 19 h). After blocking, membranes were sequentially incubated with rabbit polyclonal anti-GFP antibody (Abcam Inc., 1:5000 dilution as directed by manufacturer) and HRP-conjugated secondary antibody (Sigma, 1:2400 dilution as recommended by manufacturer). Protein bands were visualized with enhanced chemiluminescence (Pierce ECL, Thermo Scientific).

Data Analysis and Modeling

Single-channel ramp data were analyzed for Cav2.2/TN-XL unitary current and open probability using custom MATLAB programs¹⁰. For the analysis, all patches contained 1 or 2 active channels. TIRF fluorescent signals from Cav2.2/TN-XL were modeled using custom MATLAB scripts, using approaches detailed in Supplementary Methods. Generalization of the Neher-Stern equation (Eq. 1) for f values other than unity was accomplished by considering mass balance and substituting Q_1/f for Q_1 in Eq. 6 of the original Stern paper¹³.

Supplementary Material

Refer to Web version on PubMed Central for supplementary material.

Acknowledgments

Manu Ben Johny contributed valuable insights to the work. Michael Tadross created acquisition software, as well as advising on numerical simulations and Fluo 4FF imaging. The custom bath chamber for mounting cover slips was a kind gift from Luis Fernando Santana, University of Washington. Supported by a grant from the NIMH (R01 MH65531 to D.T.Y.), and from the NHLBI (Kirschstein-NRSA T32 HL07227-35 to I.E.D.).

References

1. Berridge MJ, Lipp P, Bootman MD. The versatility and universality of calcium signalling. *Nat Rev Mol Cell Biol.* 2000; 1:11–21. [PubMed: 11413485]
2. Parekh AB. Decoding cytosolic Ca²⁺ oscillations. *Trends Biochem Sci.* 2011; 36:78–87. [PubMed: 20810284]
3. Bautista DM, Lewis RS. Modulation of plasma membrane calcium-ATPase activity by local calcium microdomains near CRAC channels in human T cells. *J Physiol.* 2004; 556:805–817. [PubMed: 14966303]
4. Berkefeld H, et al. BKCa-Cav channel complexes mediate rapid and localized Ca²⁺-activated K⁺ signaling. *Science.* 2006; 314:615–620. [PubMed: 17068255]
5. Hudmon A, et al. CaMKII tethers to L-type Ca²⁺ channels, establishing a local and dedicated integrator of Ca²⁺ signals for facilitation. *J Cell Biol.* 2005; 171:537–547. [PubMed: 16275756]
6. Evans RM, Zamponi GW. Presynaptic Ca²⁺ channels--integration centers for neuronal signaling pathways. *Trends Neurosci.* 2006; 29:617–624. [PubMed: 16942804]
7. Cheng H, Lederer WJ. Calcium sparks. *Physiol Rev.* 2008; 88:1491–1545. [PubMed: 18923188]
8. Ma H, Groth RD, Wheeler DG, Barrett CF, Tsien RW. Excitation-transcription coupling in sympathetic neurons and the molecular mechanism of its initiation. *Neurosci Res.* 2011; 70:2–8. [PubMed: 21352861]

9. Dolmetsch R. Excitation-transcription coupling: signaling by ion channels to the nucleus. *Sci STKE*. 2003; 2003:PE4. [PubMed: 12538881]
10. Tadross MR, Dick IE, Yue DT. Mechanism of local and global Ca²⁺ sensing by calmodulin in complex with a Ca²⁺ channel. *Cell*. 2008; 133:1228–1240. [PubMed: 18585356]
11. Augustine GJ, Santamaria F, Tanaka K. Local calcium signaling in neurons. *Neuron*. 2003; 40:331–346. [PubMed: 14556712]
12. Sherman A, Keizer J, Rinzel J. Domain model for Ca²⁺-inactivation of Ca²⁺ channels at low channel density. *Biophys J*. 1990; 58:985–995. [PubMed: 2174274]
13. Stern MD. Buffering of calcium in the vicinity of a channel pore. *Cell Calcium*. 1992; 13:183–192. [PubMed: 1315621]
14. Simon SM, Llinas RR. Compartmentalization of the submembrane calcium activity during calcium influx and its significance in transmitter release. *Biophys J*. 1985; 48:485–498. [PubMed: 2412607]
15. Fogelson AL, Zucker RS. Presynaptic calcium diffusion from various arrays of single channels. Implications for transmitter release and synaptic facilitation. *Biophys J*. 1985; 48:1003–1017. [PubMed: 2418887]
16. Naraghi M, Neher E. Linearized buffered Ca²⁺ diffusion in microdomains and its implications for calculation of [Ca²⁺] at the mouth of a calcium channel. *J Neurosci*. 1997; 17:6961–6973. [PubMed: 9278532]
17. Klingauf J, Neher E. Modeling buffered Ca²⁺ diffusion near the membrane: implications for secretion in neuroendocrine cells. *Biophys J*. 1997; 72:674–690. [PubMed: 9017195]
18. Schneggenburger R, Neher E. Intracellular calcium dependence of transmitter release rates at a fast central synapse. *Nature*. 2000; 406:889–893. [PubMed: 10972290]
19. Sugimori M, Lang EJ, Silver RB, Llinas R. High-resolution measurement of the time course of calcium-concentration microdomains at squid presynaptic terminals. *Biol Bull*. 1994; 187:300–303. [PubMed: 7841233]
20. DeMaria CD, Soong TW, Alseikhan BA, Alvania RS, Yue DT. Calmodulin bifurcates the local Ca²⁺ signal that modulates P/Q-type Ca²⁺ channels. *Nature*. 2001; 411:484–489. [PubMed: 11373682]
21. Liang H, et al. Unified mechanisms of Ca²⁺ regulation across the Ca²⁺ channel family. *Neuron*. 2003; 39:951–960. [PubMed: 12971895]
22. Dick IE, et al. A modular switch for spatial Ca²⁺ selectivity in the calmodulin regulation of Ca^v channels. *Nature*. 2008; 451:830–834. [PubMed: 18235447]
23. Borst JG, Sakmann B. Calcium current during a single action potential in a large presynaptic terminal of the rat brainstem. *J Physiol*. 1998; 506 (Pt 1):143–157. [PubMed: 9481678]
24. Stanley EF. Single calcium channels and acetylcholine release at a presynaptic nerve terminal. *Neuron*. 1993; 11:1007–1011. [PubMed: 8274272]
25. Weber AM, et al. N-type Ca²⁺ channels carry the largest current: implications for nanodomains and transmitter release. *Nat Neurosci*. 2011; 13:1348–1350. [PubMed: 20953196]
26. Grynkiewicz G, Poenie M, Tsien RY. A new generation of Ca²⁺ indicators with greatly improved fluorescence properties. *J Biol Chem*. 1985; 260:3440–3450. [PubMed: 3838314]
27. Schermelleh L, Heintzmann R, Leonhardt H. A guide to super-resolution fluorescence microscopy. *J Cell Biol*. 2010; 190:165–175. [PubMed: 20643879]
28. Song LS, Sham JS, Stern MD, Lakatta EG, Cheng H. Direct measurement of SR release flux by tracking ‘Ca²⁺ spikes’ in rat cardiac myocytes. *J Physiol (Lond)*. 1998; 512:677–691. [PubMed: 9769413]
29. Axelrod D, Thompson NL, Burghardt TP. Total internal reflection fluorescent microscopy. *J Microsc*. 1983; 129:19–28. [PubMed: 6827590]
30. Demuro A, Parker I. Imaging single-channel calcium microdomains. *Cell Calcium*. 2006; 40:413–422. [PubMed: 17067668]
31. Navedo MF, Amberg GC, Nieves M, Molkenin JD, Santana LF. Mechanisms underlying heterogeneous Ca²⁺ sparklet activity in arterial smooth muscle. *J Gen Physiol*. 2006; 127:611–622. [PubMed: 16702354]

32. Wang MC, et al. 3D structure of the skeletal muscle dihydropyridine receptor. *J Mol Biol.* 2002; 323:85–98. [PubMed: 12368101]
33. Syngge EH. A suggested method for extending microscopic resolution into the ultramicroscopic region. *Philosophical Magazine.* 1928; 6:356–362.
34. Blinks JR, Wier WG, Hess P, Prendergast FG. Measurement of Ca²⁺ concentrations in living cells. *Prog Biophys Mol Biol.* 1982; 40:1–114. [PubMed: 6758036]
35. Brini M, et al. Nuclear Ca²⁺ concentration measured with specifically targeted recombinant aequorin. *Embo J.* 1993; 12:4813–4819. [PubMed: 8223490]
36. Montero M, et al. Monitoring dynamic changes in free Ca²⁺ concentration in the endoplasmic reticulum of intact cells. *Embo J.* 1995; 14:5467–5475. [PubMed: 8521803]
37. Rizzuto R, Simpson AW, Brini M, Pozzan T. Rapid changes of mitochondrial Ca²⁺ revealed by specifically targeted recombinant aequorin. *Nature.* 1992; 358:325–327. [PubMed: 1322496]
38. Tour O, et al. Calcium Green FAsH as a genetically targeted small-molecule calcium indicator. *Nat Chem Biol.* 2007; 3:423–431. [PubMed: 17572670]
39. Hadley RW, Lederer WJ. Properties of L-type calcium channel gating current in isolated guinea pig ventricular myocytes. *J Gen Physiol.* 1991; 98:265–285. [PubMed: 1658192]
40. Miyawaki A, et al. Fluorescent indicators for Ca²⁺ based on green fluorescent proteins and calmodulin. *Nature.* 1997; 388:882–887. [PubMed: 9278050]
41. Tallini YN, et al. Imaging cellular signals in the heart in vivo: Cardiac expression of the high-signal Ca²⁺ indicator GCaMP2. *Proc Natl Acad Sci U S A.* 2006; 103:4753–4758. [PubMed: 16537386]
42. Heim N, Griesbeck O. Genetically encoded indicators of cellular calcium dynamics based on troponin C and green fluorescent protein. *J Biol Chem.* 2004; 279:14280–14286. [PubMed: 14742421]
43. Mori MX, Erickson MG, Yue DT. Functional stoichiometry and local enrichment of calmodulin interacting with Ca²⁺ channels. *Science.* 2004; 304:432–435. [PubMed: 15087548]
44. Mank M, et al. A FRET-based calcium biosensor with fast signal kinetics and high fluorescence change. *Biophys J.* 2006; 90:1790–1796. [PubMed: 16339891]
45. Colecraft HM, Brody DL, Yue DT. G-protein inhibition of N- and P/Q-type calcium channels: distinctive elementary mechanisms and their functional impact. *J Neurosci.* 2001; 21:1137–1147. [PubMed: 11160384]
46. Noceti F, et al. Effective gating charges per channel in voltage-dependent K⁺ and Ca²⁺ channels. *J Gen Physiol.* 1996; 108:143–155. [PubMed: 8882860]
47. Jones LP, DeMaria CD, Yue DT. N-type calcium channel inactivation probed by gating-current analysis. *Biophys J.* 1999; 76:2530–2552. [PubMed: 10233069]
48. Tay LH, Griesbeck O, Yue DT. Live-Cell Transforms between Ca²⁺ Transients and FRET Responses for a Troponin-C-Based Ca²⁺ Sensor. *Biophys J.* 2007; 93:4031–4040. [PubMed: 17704158]
49. Fang K, Colecraft HM. Mechanism of auxiliary {beta}-subunit-mediated membrane targeting of L-type (CaV1.2) channels. *J Physiol.* 2011; 589:4437–4455. [PubMed: 21746784]
50. Linse S, Helmerson A, Forsen S. Calcium binding to calmodulin and its globular domains. *J Biol Chem.* 1991; 266:8050–8054. [PubMed: 1902469]
51. Martin SR, Andersson Telemann A, Bayley PM, Drakenberg T, Forsen S. Kinetics of calcium dissociation from calmodulin and its tryptic fragments. A stopped-flow fluorescence study using Quin 2 reveals a two-domain structure. *Eur J Biochem.* 1985; 151:543–550. [PubMed: 4029146]
52. Chaudhuri D, Issa JB, Yue DT. Elementary mechanisms producing facilitation of Cav2.1 (P/Q-type) channels. *J Gen Physiol.* 2007; 129:385–401. [PubMed: 17438119]
53. Koushik SV, Chen H, Thaler C, Puhl HL 3rd, Vogel SS. Cerulean, Venus, and VenusY67C FRET reference standards. *Biophys J.* 2006; 91:L99–L101. [PubMed: 17040988]
54. Erickson MG, Alseikhan BA, Peterson BZ, Yue DT. Preassociation of calmodulin with voltage-gated Ca(2+) channels revealed by FRET in single living cells. *Neuron.* 2001; 31:973–985. [PubMed: 11580897]

55. Long SB, Campbell EB, Mackinnon R. Crystal structure of a mammalian voltage-dependent Shaker family K⁺ channel. *Science*. 2005; 309:897–903. [PubMed: 16002581]
56. Blunck R, Starace DM, Correa AM, Bezanilla F. Detecting rearrangements of shaker and NaChBac in real-time with fluorescence spectroscopy in patch-clamped mammalian cells. *Biophys J*. 2004; 86:3966–3980. [PubMed: 15189893]
57. Viard P, et al. PI3K promotes voltage-dependent calcium channel trafficking to the plasma membrane. *Nat Neurosci*. 2004; 7:939–946. [PubMed: 15311280]
58. Altier C, et al. ORL1 receptor-mediated internalization of N-type calcium channels. *Nat Neurosci*. 2006; 9:31–40. [PubMed: 16311589]
59. Green EM, Barrett CF, Bultynck G, Shamah SM, Dolmetsch RE. The tumor suppressor eIF3e mediates calcium-dependent internalization of the L-type calcium channel CaV1.2. *Neuron*. 2007; 55:615–632. [PubMed: 17698014]
60. Kits KS, de Vlieger TA, Kooi BW, Mansvelder HD. Diffusion barriers limit the effect of mobile calcium buffers on exocytosis of large dense cored vesicles. *Biophys J*. 1999; 76:1693–1705. [PubMed: 10049349]

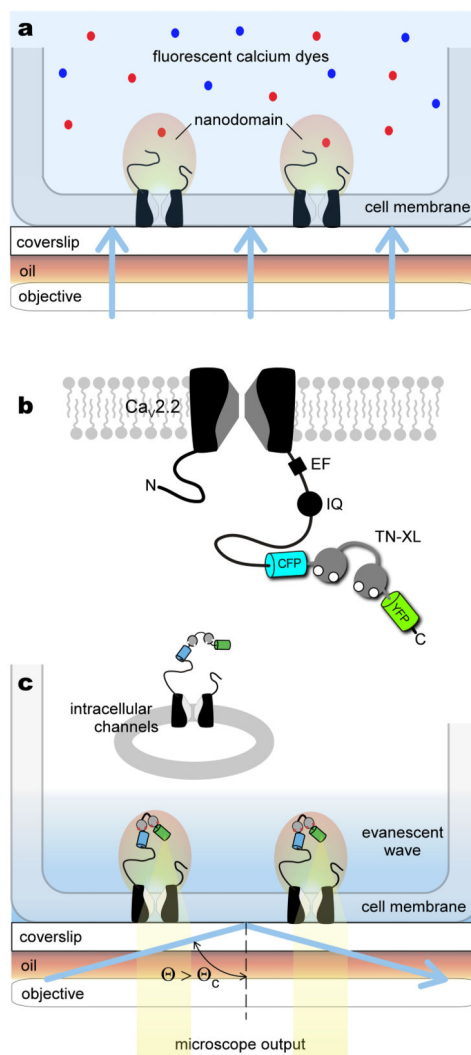


Figure 1. Approach to resolving channel nanodomain Ca^{2+} signals

a. Conventional wide-field imaging using cytosolic chemical fluorescent dyes cannot resolve channel nanodomain Ca^{2+} signals. Blue shading denotes region of fluorescence excitation, which extends throughout the cell under wide-field imaging. **b.** Design of the genetically encoded Ca^{2+} indicator TN-XL fused to the carboxy tail of the α_{1B} subunit of a $\text{Ca}_v2.2$ channel, yielding $\text{Ca}_v2.2/\text{TN-XL}$. For orientation, structure-function elements involved in calmodulin regulation are denoted on carboxy terminus²¹: EF, EF-hand region; IQ, IQ-domain for apoCaM binding. CFP denotes enhanced CFP. YFP denotes circularly permuted Citrine. **c.** $\text{Ca}_v2.2/\text{TN-XL}$ constructs act as a 'near-field' sensor of nanodomain Ca^{2+} . TIRF imaging evanescent wave illuminates only $\text{Ca}_v2.2/\text{TN-XL}$ channels within ~150 nm from the glass/cell membrane interface, as indicated by the blue-shaded region. This mode of excitation potentially excludes intracellular channels from consideration. When laser illumination angle Θ exceeds a critical angle Θ_c , TIRF illumination occurs.

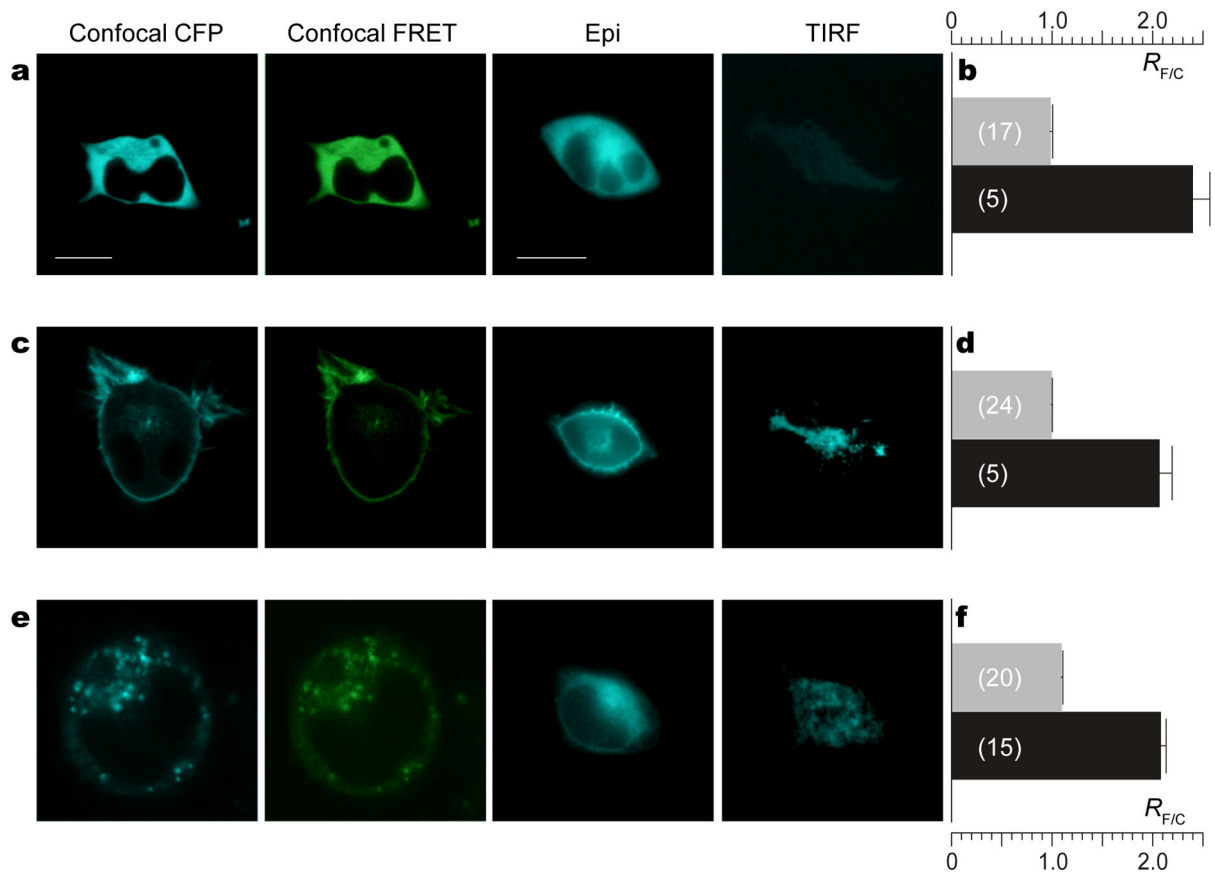


Figure 2. Ca_v2.2/TN-XL fusion construct preserves function of sensor

a, Behavior of free TN-XL. Left to right: Confocal (CFP filter), confocal (FRET filter), epifluorescence (CFP filter), and TIRF (CFP filter) images of HEK293 cells expressing cytoplasmic TN-XL. White scale bar indicates 10 μ M. Bar at far left pertains to all confocal images. Bar at middle right pertains to all epifluorescence and TIRF images. **b**, TN-XL ratio ($R_{F/C} = S_F/S_C$) measured in resting cells (R_{min}) (gray bars) and in cells under high Ca^{2+} (R_{max}) (black bars). Data shown as mean \pm sem with number of cells in parentheses. **c** and **d**, Behavior of TN-XL-Ras (membrane targeted TN-XL). Format as in **a** and **b**, respectively. **e** and **f**, Behavior of Ca_v2.2/TN-XL (N-type channel fused to TN-XL). Format as in **a** and **b**, respectively.

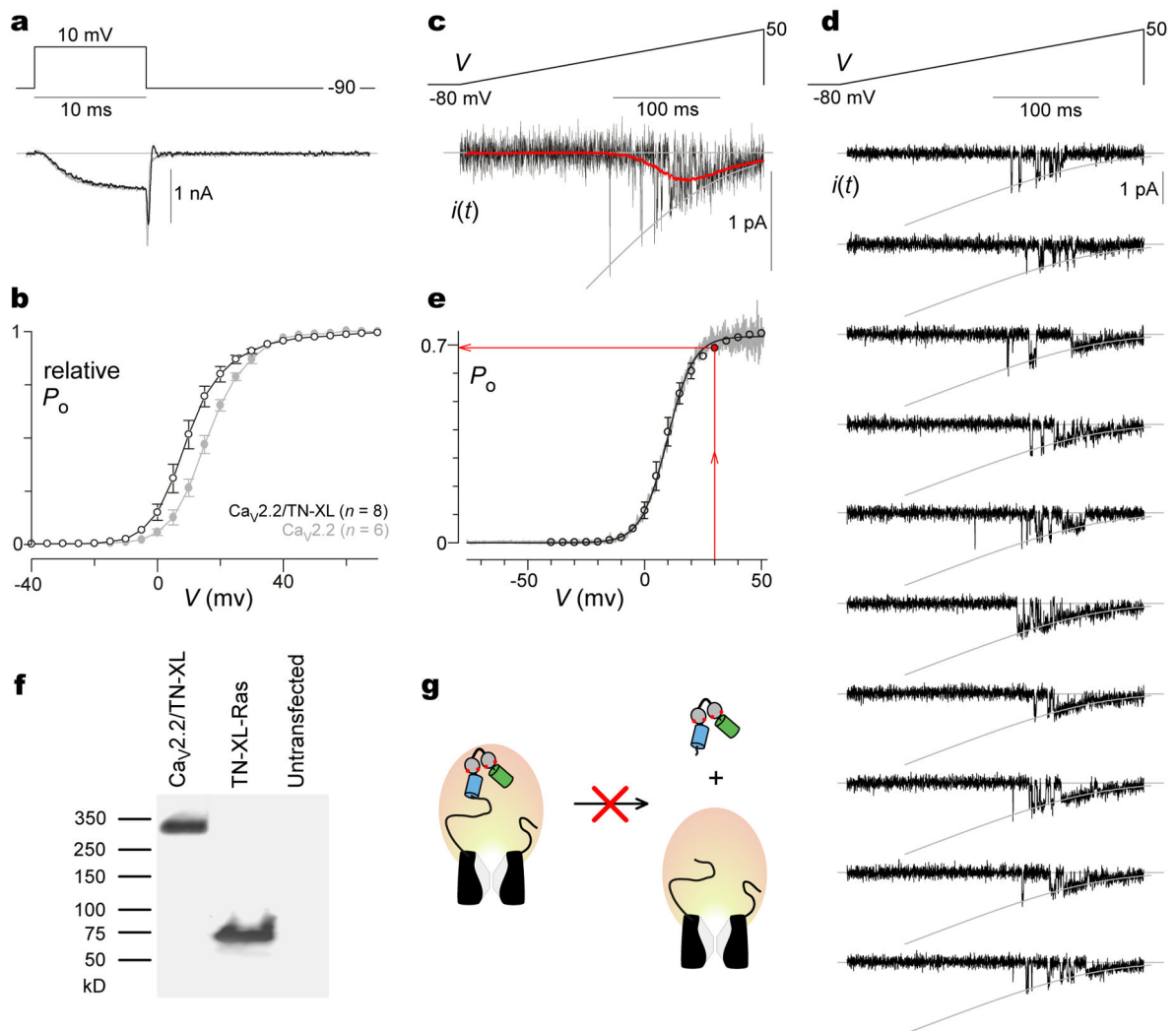


Figure 3. $\text{Ca}_V2.2/\text{TN-XL}$ fusion construct preserves function of channel

a, Exemplar whole-cell currents of HEK293 cells expressing $\text{Ca}_V2.2$ channels (gray) or $\text{Ca}_V2.2/\text{TN-XL}$ channels (black), using 10 mM Ca^{2+} as charge carrier, and 10 mM EGTA intracellular Ca^{2+} buffering. **b**, Whole-cell tail-activation curves of $\text{Ca}_V2.2$ (gray) and $\text{Ca}_V2.2/\text{TN-XL}$ (black), obtained from records as in **a**. Data shown as mean \pm sem with number of cells in parentheses. **c**, Single-channel analysis of $\text{Ca}_V2.2/\text{TN-XL}$. Top, On-cell ramp-voltage waveform delivered every 5–15 s. Bottom, Exemplar single-channel sweep shown at high-gain magnification (100–200/patch). 90 mM Ba^{2+} as charge carrier; 2 kHz lowpass filtering. Leak-subtracted traces were averaged, yielding red I - V curve. Unitary current relation (convex gray curve) was fitted to the open-channel current level using GHK equation¹⁰. **d**, Multiple exemplar single-channel sweeps from another patch, shown at lower-gain magnification to impart a sense of the overall reproducibility and excellent resolution of elementary events. Format as in **c**. **e**, Single-channel P_O - V relation (gray, with fit in black, average of $n = 4$ patches), determined by dividing I - V curve (**c**, red trace) by unitary current relation (**c**, gray GHK fit). P_O - V curve was calibrated in voltage by aligning the single-channel activation curve with the whole-cell curve reproduced from **b** (open

circles). From calibrated P_O - V curve, the P_o at 30 mV is 0.69. **f**, Immunoblots of HEK293 cell lysates probed with anti-GFP antibody; (left) Ca_v2.2/TN-XL at ~320 kD; (middle) TN-XL-Ras at ~71 kD; (right) control (untransfected) cells for reference. **g**, Lack of lower molecular-weight species in leftmost lane of panel **f** excludes proteolysis of sensor from channel.

Author Manuscript

Author Manuscript

Author Manuscript

Author Manuscript

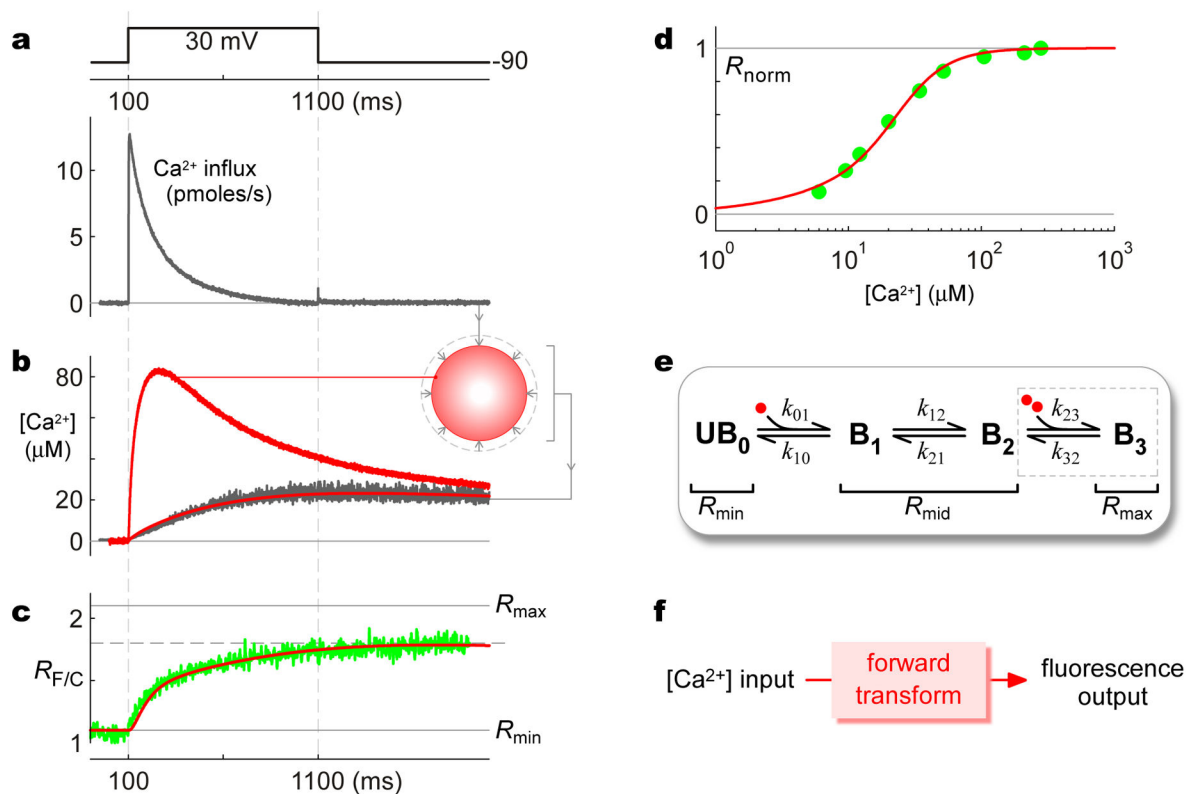


Figure 4. Calibration of Ca_v2.2/TN-XL fusion construct

a, High-amplitude Ca²⁺ influx into HEK293 cell expressing Ca_v2.2 channels, observed with 10 mM external Ca²⁺ and minimal internal Ca²⁺ buffering of 1 mM EGTA. **b**, Simultaneous [Ca²⁺] measurement (dark trace) deduced from 10 μM Fluo-4FF Ca²⁺-indicator fluorescence from entirety of same cell (514 nm excitation, 545 nm emission). Ca²⁺ determination rendered ratiometric by inclusion of 2.5 μM red Alexa 568 dye (514 nm excitation, 580 nm long-pass emission). Inset, cartoon of spatial Ca²⁺ gradients in this cell. Red traces, projected [Ca²⁺] waveforms from Ca²⁺ diffusion mechanism constrained by Ca²⁺ input in **a** and aggregate [Ca²⁺] (dark trace): lower red trace, aggregate [Ca²⁺]; upper red trace, submembranous [Ca²⁺]. **c**, Average FRET-ratio ($R_{F/C}$) response of Ca_v2.2/TN-XL channels in TIRF volume (green trace); same protocol as in **a** and **b**. Red trace, output of TN-XL forward transform in **e**, when driven by submembranous [Ca²⁺] input (**b**, upper red trace). **d**, Normalized steady-state FRET-ratio response ($R_{\text{norm}} = (R_{F/C} - R_{\text{min}})/(R_{\text{max}} - R_{\text{min}})$) of Ca_v2.2/TN-XL to [Ca²⁺] (experimental green symbols). Red trace, steady-state output of TN-XL forward transform in **e**, when driven by differing fixed [Ca²⁺]. **e**, State-diagram representation of Ca_v2.2/TN-XL. Red circles, Ca²⁺ ions. **f**, System of states and corresponding fluorescence/FRET properties constitutes a forward transform that predicts TN-XL sensor outputs as a function of time-varying Ca²⁺ inputs.

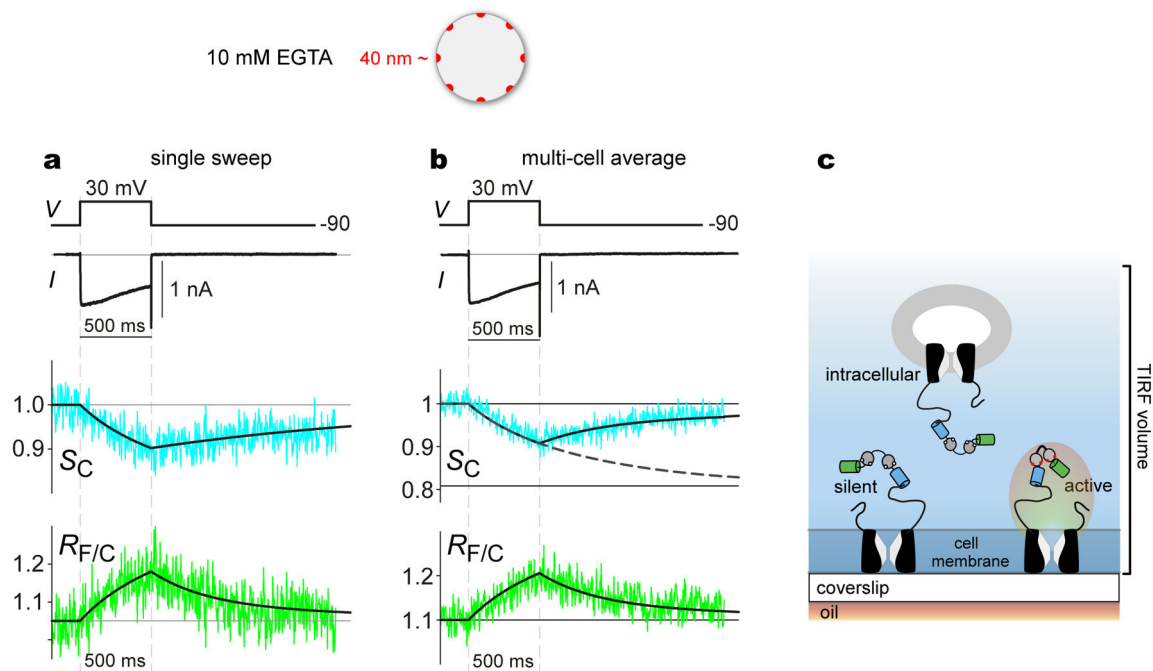


Figure 5. $\text{Ca}_v2.2/\text{TN-XL}$ sensors respond to channel nanodomain Ca^{2+} signals

Top cartoon, Ca^{2+} nanodomains under elevated Ca^{2+} buffering, where Ca^{2+} elevation is restricted to nanodomains, each affiliated with individual channel. 40 nm nanodomain calculated with Equation 1, $f = 1$ (classical assumption), unitary current $i = 0.085$ pA, and conservatively requiring $[\text{Ca}^{2+}] \sim 60$ nM (the approximate resting physiological Ca^{2+} concentration). **a**, Simultaneous records of whole-cell current (top) and TIRF fluorescence signals (middle and bottom) from HEK293 cell expressing $\text{Ca}_v2.2/\text{TN-XL}$, using 10 mM external Ca^{2+} and 10 mM internal EGTA Ca^{2+} buffering. Shown are data from a single trial, evoked by the first step depolarization in the cell. Top, Voltage and current waveforms, with moderately-sized current chosen to minimize buffer consumption. Middle, Corresponding CFP fluorescence signal after normalization to baseline level (S_C , noisy trace). Black curve, approximate exponential fits (initial phase: 200 ms (10%), 880 ms (90%); recovery phase: 2000 ms (100%)). Vertical ticks, 0.1 increment. Bottom, Corresponding FRET-ratio signal ($R_{F/C}$, noisy trace). Black curve, approximate exponential fits (initial phase: 200 ms (10%), 880 ms (90%); recovery phase: 400 msec (70%), 2000 ms (30%)). Vertical ticks, 0.1 increment. **b**, Average $\text{Ca}_v2.2/\text{TN-XL}$ responses to nanodomain Ca^{2+} signals, as isolated with 10 mM internal EGTA Ca^{2+} buffering. Protocol and format as in panel **a**. $n = 4$ cells, with records taken from the first step depolarization delivered in cells. CDI sometimes increased with repeated depolarizations, reflecting buffer depletion with attendant slowing of $R_{F/C}$ waveform decay. Cells exhibiting peak currents > 500 pA were not considered, as these cells demonstrated negligible $R_{F/C}$ transients, presumably reflecting insufficient trafficking of active channels. Solid-black-curve exponential fits were similar, with S_C exponential fit (initial phase: 200 ms (10%), 880 ms (90%); recovery phase: 500 ms (80%), 2500 ms (20%)), and $R_{F/C}$ fit (initial phase: 200 ms (10%), 880 ms (90%); recovery phase: 400 msec (70%), 2000 ms (30%)). Dashed black curve, continuation of initial phase S_C exponential fit, which asymptotes at lower horizontal black line in middle. **c**, Schematic of

various classes of $Ca_v2.2/TN-XL$ species in TIRF volume. Blue shading indicates region of excitation by evanescent wave in TIRF volume.

Author Manuscript

Author Manuscript

Author Manuscript

Author Manuscript

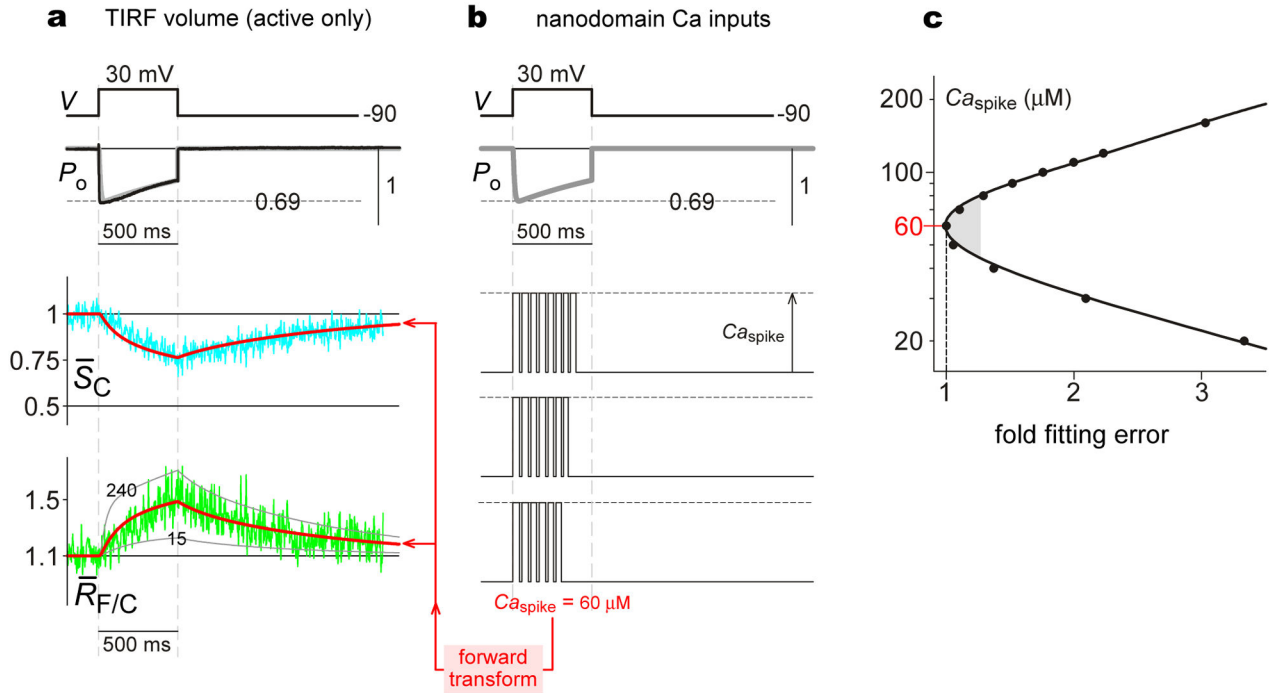


Figure 6. Estimates of nanodomain Ca^{2+} amplitude from $Ca_v2.2/TN-XL$ responses
a. Average $Ca_v2.2/TN-XL$ responses to nanodomain Ca^{2+} signals, corrected to reflect signal of active channels alone. Top, black trace plots average whole-current, rescaled to open probability P_O by normalizing peak current during 30-mV pulse to 0.69. Gray trace, exponential fit to P_O waveform. Middle, cyan trace plots average S_C , corrected CFP signal. Red trace, forward transform prediction of experimental S_C using $Ca_{spike} = 60 \mu M$. Bottom, Green trace plots average $R_{F/C}$, corrected FRET-ratio signal. Red trace, forward transform prediction of experimental $R_{F/C}$ using $Ca_{spike} = 60 \mu M$. Gray traces, transform prediction with Ca_{spike} as labeled. **b.** Nanodomain Ca^{2+} signals input to forward transform for prediction of $Ca_v2.2/TN-XL$ responses in **a**. Top, P_O waveform reproduced from **a**. Middle, Schematic of stochastic Ca^{2+} pulses in nanodomain. Bottom, Forward transform box with parameters in Table 1. **c.** Ca_{spike} estimation criteria. Presumed Ca_{spike} values plotted versus fold-fitting error (sum of squared deviations between fit and data, normalized to sum with $Ca_{spike} = 60 \mu M$). Cusp of plot denotes $Ca_{spike} = 60 \mu M$ as best fit. Shaded zone specifies approximate confidence region, where fits yield errors within 25% of minimum.

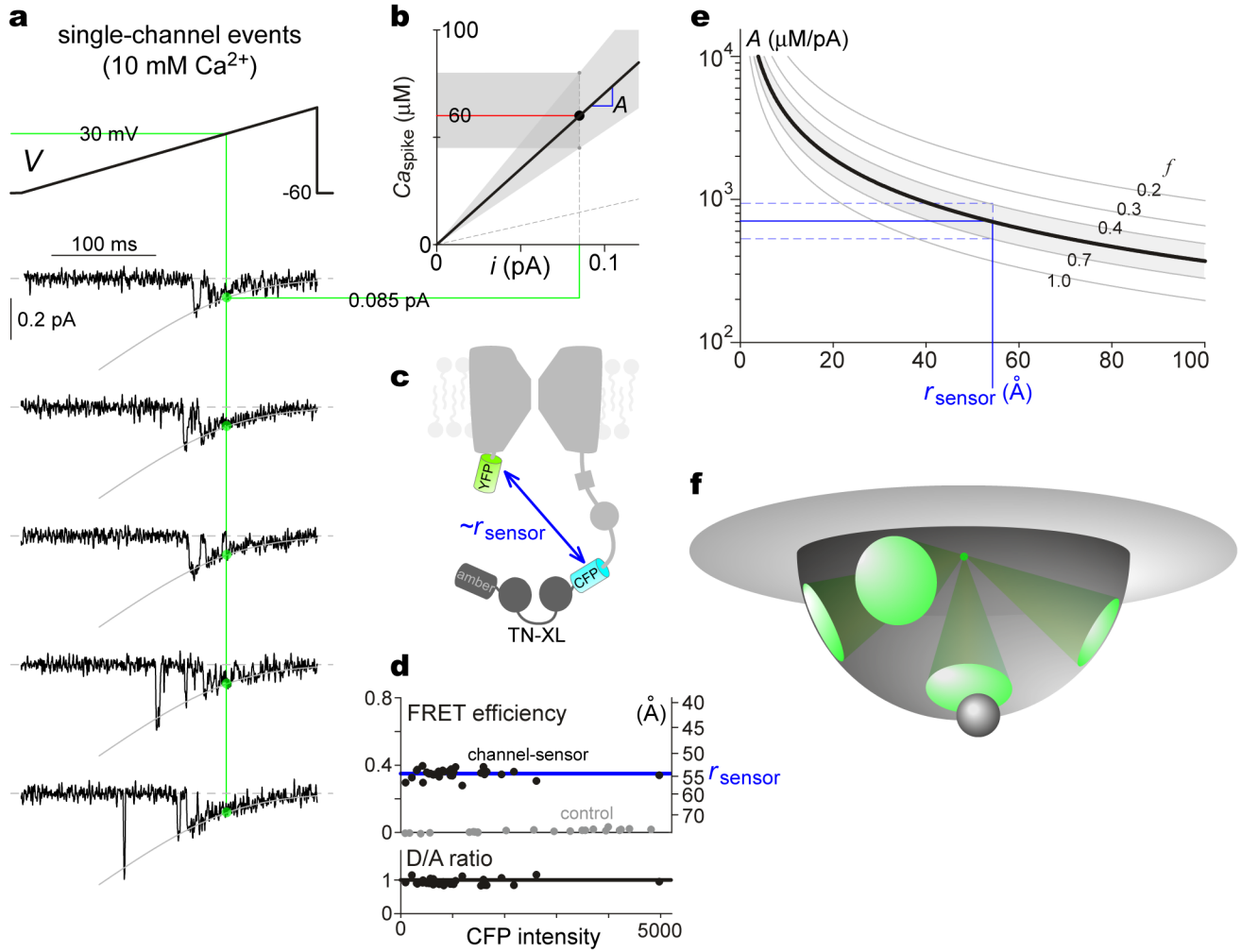


Figure 7. Potential fenestrated Ca^{2+} egress within $\text{Cav}2.2$ channel nanodomain
a, On-cell single-channel ramp experiments, except 10 mM Ca^{2+} is charge carrier to accord with whole-cell experiments; 700-Hz lowpass filtering. Voltages adjusted to align single-channel activation with whole-cell activation curves. Exemplars from single patch, with openings to GHK relation (gray curve). Unitary current i at 30 mV (green circles), 0.085 pA in 5 patches. **b**, Gain factor A , slope of Ca_{spike} versus i relation. Shading, various estimates of A over confidence range of Ca_{spike} . Sloped dashed line, lower-limit estimate of A using uncorrected data. **c**, Schematic, FRET construct to estimate r_{sensor} . Substituting circularly permuted *amber* for circularly permuted Citrine of TN-XL maintains sensor-channel configuration. **d**, Estimating r_{sensor} via FRET. Each black symbol, individual HEK293 cell expressing construct in **c**. Two outputs for each such cell obtained via 3^3 -FRET analysis⁵⁴ of fluorescence images: FRET efficiency and ratio of donor (CFP) to acceptor (YFP) molecules (D/A ratio), both plotted versus CFP intensity (\propto construct expression level). Data from cells exhibiting D/A ratio ~ 1 (as expected from **c**) are displayed and analyzed (bottom subpanel, black line at unity). Invariant FRET efficiency with increasing CFP intensity (top subpanel) excludes spurious FRET, facilitating interpretation of FRET efficiency (~ 0.35 , blue line, top subpanel, left axis) as indicative of $r_{\text{sensor}} \sim 55 \text{ \AA}$ (top

subpanel, right axis). Gray symbols, control cells expressing YFP and CFP separately, yielding efficiencies ~ 0 . **e**, A versus sensor distance from channel mouth (r_{sensor}), calculated with Neher-Stern equation (Eq. 1), using parameters^{13,60} $D_{\text{Ca}} = 0.4 \mu\text{m}^2 \text{ms}^{-1}$ and $k_{\text{Bon}} = 10^{-3} \mu\text{M}^{-1} \text{ms}^{-1}$ for EGTA. Gray curves, plots with f values as labeled. Mapping A from **b**, with r_{sensor} from **d**, yields $f \sim 0.53$ (black curve) and range (0.4–0.7, shading). **f**, Schematic, idealized fenestrated Ca^{2+} egress from inner channel mouth. Green cones, permissive radial diffusion paths from source (green dot), summing to $f \sim 0.53$. Target molecule (gray ball) within/near portal enjoys preferential signaling.

Table 1Ca_v2.2/TNXL parameters for HEK293 cells under TIRF imaging

Fluorescence Parameters ¹	Value
Ca _v 2.2/TNXL R_{\min}	1.10 ($n = 20$ cells, Fig. 2f)
Ca _v 2.2/TNXL R_{mid}	1.53 ²
Ca _v 2.2/TNXL R_{\max}	2.10 ($n = 15$ cells, Fig. 2f)
Ca _v 2.2/TNXL α_0	2.00 ($n = 8$ cells)
Ca _v 2.2/TNXL α_1	1.57 ³

Kinetic Parameters ⁴	Value
k_{01}	174.4 ms ⁻¹ M ⁻¹
k_{10}	0.00239 ms ⁻¹
k_{12}	0.00174 ms ⁻¹
k_{21}	0.00309 ms ⁻¹
k_{23}	0.126 × 10 ⁶ ms ⁻¹ M ⁻²
k_{32}	1/733 ms ⁻¹

¹ Fluorescence parameters obtained following experimental procedures used to characterize TN-L15⁴⁸, unless specified otherwise.

^{2,4} Set by global fitting of Fig. 4e scheme to data Figs. 4a, 4c, and 4d.

³ Linear interpolation on R values. Explicitly, $\alpha_1 = \alpha_0 - (R_{\text{mid}} - R_{\min}) / (R_{\max} - R_{\min})$.